PAPER WITH FULL DATA ATTACHED

Open Access

Nationwide urban ground deformation in Japan for 15 years detected by ALOS and Sentinel-1

Yu Morishita[1*] , Ryu Sugimoto[1], Ryosuke Nakamura[1], Chiaki Tsutsumi[1], Ryo Natsuaki[2] and Masanobu Shimada[3]

Abstract

InSAR time series analysis has become a major tool for nationwide land deformation monitoring. Sentinel-1 SAR data have enabled us to measure and monitor ground deformation globally with high accuracy and resolution through InSAR time series analysis, due to its constant and frequent global coverage and open data policy since 2014. Although several datasets from previous SAR satellites were available before Sentinel-1, such comprehensive deformation monitoring was not performed due to several limitations such as data quality, analysis technique, data policy, and processing capacity at that time. However, since a large amount of ALOS InSAR products and an open-source InSAR time series analysis tool LiCSBAS have become openly and freely available, we can easily derive the deformation from 2006 to 2011 by using them. In this study, we detected the deformation time series and velocity in all major urban areas in Japan from 2006 to 2011 and compared the results with the deformation from 2014 to 2020 detected by Sentinel-1 data. The two deformation datasets with different time periods revealed various 15-year deformation histories, such as long-term constant subsidence in Tomakomai and Niigata, changes in deformation areas and/ or velocities in Hirosaki, Kujyukuri, Kanazawa, and Matsushiro, and appearance or disappearance of deformation in Joso, Yoyogi, and Kyoto. Future abundant and continuous SAR data acquisitions will reveal more long-term deformation transitions and help to understand the details of the mechanisms.

Keywords ALOS, Ground deformation, InSAR, Japan, Nationwide, Sentinel-1, Subsidence, Time series analysis

*Correspondence:
Yu Morishita
asobu.morimori@gmail.com
[1] Digital Architecture Research Center, National Institute of Advanced Industrial Science and Technology, 2-4-7 Aomi, Koto-ku, Tokyo 135-0064, Japan
[2] Department of Electrical Engineering and Information Systems, The University of Tokyo, 7-3-1 Hongo, Bunkyo-ku, Tokyo 113-8656, Japan
[3] Division of Architectural, Civil and Environmental Engineering, School of Science and Engineering, Tokyo Denki University, Ishizaka, Hatoyama-machi, Hiki-gun, Saitama 350-0394, Japan

1 Introduction

Since the launch of Sentinel-1 in 2014, several activities to measure or monitor the large-scale ground deformation at high resolution using Synthetic Aperture Radar Interferometry (InSAR) time series analysis have been proposed and operationalized (e.g., Crosetto et al. 2020; Lazecký et al. 2020; Morishita 2021) due to the global, continuous, frequent, and freely available Sentinel-1 data. However, before Sentinel-1, such operational large-scale deformation monitoring was very rare due to several limitations, such as the amount and quality of the available Synthetic Aperture Radar (SAR) data (e.g., orbit control, observation frequency, swath width, orbit information accuracy), the immaturity of the analysis technique, the accessibility of the data, and the computational power to

process huge amounts of data (Chaussard et al. 2013; Elliott et al. 2016).

In 2022, the National Institute of Advanced Industrial Science and Technology (AIST) Advanced Land Observing Satellite (ALOS) InSAR products were released as an open and free dataset (Sugimoto et al. 2021). The products include ∼ 500 thousand interferograms from 2006 to 2011 covering Japan, the Philippines, Indonesia (except the islands of Borneo and New Guinea), Nepal, Turkey, the East African Rift, and the west coast of North America as of July 2023. Since unwrapped data are available for all interferograms, they can be easily used for InSAR time series analysis. In addition, an open-source InSAR time series analysis tool, LiCSBAS, was released in 2020, which allows us to semi-automatically and easily derive the deformation time series and velocity from the stack of unwrapped interferograms (Morishita et al. 2020).

Morishita (2021) derived the deformation time series and velocity in all major urban areas in Japan from 2014 to 2020 using Sentinel-1 interferograms and LiCSBAS. Further historical deformation information would be useful for understanding the mechanism and taking countermeasures if necessary. In this study, we detected deformation in Japan from 2006 to 2011 using ALOS InSAR products and LiCSBAS. In addition, we compared the deformations in two different periods and discussed the 15-year deformation history.

2 Data and methods
2.1 Areas of interest
The same 73 urban areas as in Morishita (2021) were selected as areas of interest (AOIs) in this study based on the densely inhabited district (DID; Ministry of Land, Infrastructure, Transport and Tourism 2015) metric (Table 1, Fig. 1), namely meeting at least one of the following conditions:

(1) If the DID has a population of ≥ 100,000.
(2) If the DID has a population of < 100,000 but close to (1).
(3) If the DID is located in one of the 47 prefectural capitals.
(4) If leveling surveys have been conducted continuously in the DID (Ministry of the Environment 2020).
(5) If significant deformation has been detected in the DID in previous studies (e.g., Morishita et al. 2020).

The three-digit AOI ID is also the same as Morishita (2021) (i.e., two-digit prefectural ID (01–47) and a single-digit sub-number (1–7)). Six sub-AOIs were added to clearly describe the locations of detected deformation in 131 Kanto, 201 Nagano, and 271 Osaka (Table 1).

The area of 431 Kumamoto was contracted to fit the DID in this study because the area in Morishita (2021) was expanded to detect the broad postseismic deformation caused by the 2016 Kumamoto earthquake sequence. The northern area of 131 Kanto, which could not be covered by two frames of ALOS, was also shortened compared with Morishita (2021).

2.2 Data
We used the AIST ALOS InSAR products (Sugimoto et al. 2021). They were published on AI Bridging Cloud Infrastructure (ABCI) in April 2022 under the Creative Commons (CC) BY 4.0 license and can be freely downloaded. The products consist of all possible pairs of interferograms using all available data observed by ALOS from February 2006 to April 2011. The interferometric processing and phase unwrapping were performed by SigmaSAR (Shimada 2018) and Statistical-Cost, Network-Flow Algorithm for Phase Unwrapping (SNAPHU; Chen and Zebker 2002), respectively. The digital elevation model (DEM) used is Advanced Spaceborne Thermal Emission and Reflection Radiometer (ASTER) Global Digital Elevation Model (GDEM) ver2 (Tachikawa et al. 2011). The geocoded image has a pixel spacing of 0.0003 degrees (∼ 30 m).

Only the frames with the off-nadir angle of 34.3° were used because there are not enough images with other off-nadir angles. The frames covering more than half of each AOI in both ascending (path ID 394–432) and descending (path ID 052–077) orbits were selected for processing. Since the swath width of each frame is ∼ 70 km and there is an overlap area of ∼ 30 km between adjacent paths, about half of the AOIs are covered by multiple paths with slightly different incidence angles (Additional file 1: Table S1). Only the descending path 062 (covering 202 Matsumoto, 231 Nagoya, and 232 Toyohashi) was excluded from processing because the number of available epochs (5 epochs) and the total period (< 1.3 years) were insufficient to achieve significant accuracy for time series analysis. Consequently, all AOIs except 232 Toyohashi have both ascending and descending data.

Three large AOIs (i.e., 131 Kanto, 213 Nagoya, and 271 Osaka) require two consecutive frames to cover the entire area. To mitigate the discontinuity of the time series result at the frame boundary, the unwrapped data of the two frames were concatenated before the time series analysis by compensating the biases from the average of the difference of the unwrapped phases in the overlapping area between frames. Their frame IDs are modified in this paper (e.g., the concatenated frame ID of 404_0700_343 and 404_0710_343 is 404_0702_343) to distinguish them from single frames (Additional file 1: Table S1).

Table 1 AOI list and detected deformation signals

AOI ID	Main City Name	Deformation[a]		Figures
		ALOS (2006–2011)	Sentinel-1 (2014–2020)	
011	Sapporo	(S): 5 mm/year	(S): 5 mm/year	
012	Hakodate			
013	Asahikawa			
014	Kushiro	(S): 5 mm/year		
015	Obihiro			
016	Tomakomai	(S): 10 mm/year	(S): 10 mm/year	2
021	Aomori		S: 5 mm/year	
022	Hirosaki	(S): 40 mm/year	(S): 40 mm/year	4
023	Hachinohe			
031	Morioka			
041	Sendai			
042	Kesennuma		(S): 10 mm/year	
043	Osaki			
051	Akita			
061	Yamagata		S: 5 mm/year	
062	Yonezawa			
071	Fukushima			
072	Koriyama			
131	Kanto		S: 10 mm/year U: 5 mm/year	
- 081	- Joso	(S): 5 mm/year		8
- 121	- Kujyukuri	S: 5 mm/year (S): 15 mm/year (U): 5 mm/year	S: 5 mm/year (S): 20 mm/year (U): 5 mm/year	5
- 132	- Yoyogi	U: 5 mm/year		9
- 141	- Hakone	(S): 10 mm/year		14
151	Niigata	S: 10 mm/year	S: 15 mm/year	3
152	Nagaoka	(S): 5 mm/year	(S): 5 mm/year	
153	Sanjo		S: 25 mm/year	
154	Kashiwazaki	P: 5 mm/year[b]	S: 5 mm/year	12
155	Ojiya			15
156	Joetsu			
157	Minamiuonuma			
161	Toyama			
171	Kanazawa	S: 5 mm/year (S): 10 mm/year	S: 5 mm/year (S): 10 mm/year	6
172	Nanao			
181	Fukui			
191	Kofu			
201	Nagano			10
- 203	Matsushiro	(S): 5 mm/year	(S): 10 mm/year	7
202	Matsumoto			
211	Gifu			
221	Shizuoka		(S): 5 mm/year	
222	Hamamatsu	(S): 5 mm/year	(S): 15 mm/year	
223	Numazu		(S): 5 mm/year	
224	Fuji		(S): 5 mm/year	
231	Nagoya		(S): 15 mm/year	

Table 1 (continued)

AOI ID	Main City Name	Deformation[a]		Figures
		ALOS (2006–2011)	Sentinel-1 (2014–2020)	
232	Toyohashi			
241	Tsu		(S): 5 mm/year	
242	Yokkaichi	S: 5 mm/year	(S): 5 mm/year	
251	Otsu		(S): 5 mm/year	
261	Kyoto	U: 5 mm/year	(S): 15 mm/year	11
271	Osaka	S: 30 mm/year	(S): 15 mm/year	
- 272	- Arima-Takatsuki		U: 5 mm/year	13
281	Kobe		(S): 20 mm/year	
282	Himeji		S: 5 mm/year	
283	Toyooka			
291	Nara		U: 5 mm/year	
301	Wakayama		(S): 5 mm/year	
311	Tottori			
321	Matsue			
331	Okayama			
341	Hiroshima	(S): 10 mm/year	(S): 10 mm/year	
342	Fukuyama	(S): 10 mm/year	(S): 30 mm/year	
351	Yamaguchi			
352	Shimonoseki		(S): 5 mm/year	
361	Tokushima	(S): 10 mm/year	(S): 5 mm/year	
371	Takamatsu			
381	Matsuyama			
391	Kochi			
401	Fukuoka		(S): 10 mm/year	
402	Kitakyushu	(S): 5 mm/year	(S): 5 mm/year	
403	Kurume	(S): 5 mm/year	(S): 5 mm/year	
411	Saga			
421	Nagasaki		(S): 15 mm/year	
422	Sasebo		(S): 5 mm/year	
431	Kumamoto		P: 25 mm/year[b]	
441	Oita	(S): 5 mm/year	S: 5 mm/year	16
442	Beppu		S: 5 mm/year	
451	Miyazaki	(S): 5 mm/year	(S): 10 mm/year	
461	Kagoshima			
471	Naha		(S): 10 mm/year	

[a] Detected deformation. P, postseismic deformation; S, subsidence; U, uplift; (), only outside of DID

[b] Only postseismic data were used

Among the 73 AOIs, significant coseismic deformation occurred in 154 Kashiwazaki by the moment magnitude (Mw) 6.6 Niigata-ken Chuetsu-oki earthquake on July 16, 2007 (Nishimura et al. 2008a). To exclude the coseismic deformation from the time series analysis result, the data before the earthquake were excluded.

On March 11, 2011, the Mw 9.0 Tohoku earthquake occurred. Most of the AOIs in eastern Japan were affected by the large coseismic deformation, and some of them have post-earthquake data (Kobayashi et al. 2011). However, the coseismic deformation is dominated by the long-wavelength component and can be removed by the spatiotemporal filter and deramp during the time series analysis (see Sect. 2.3). Therefore, the post-earthquake data were included in the following time series analysis.
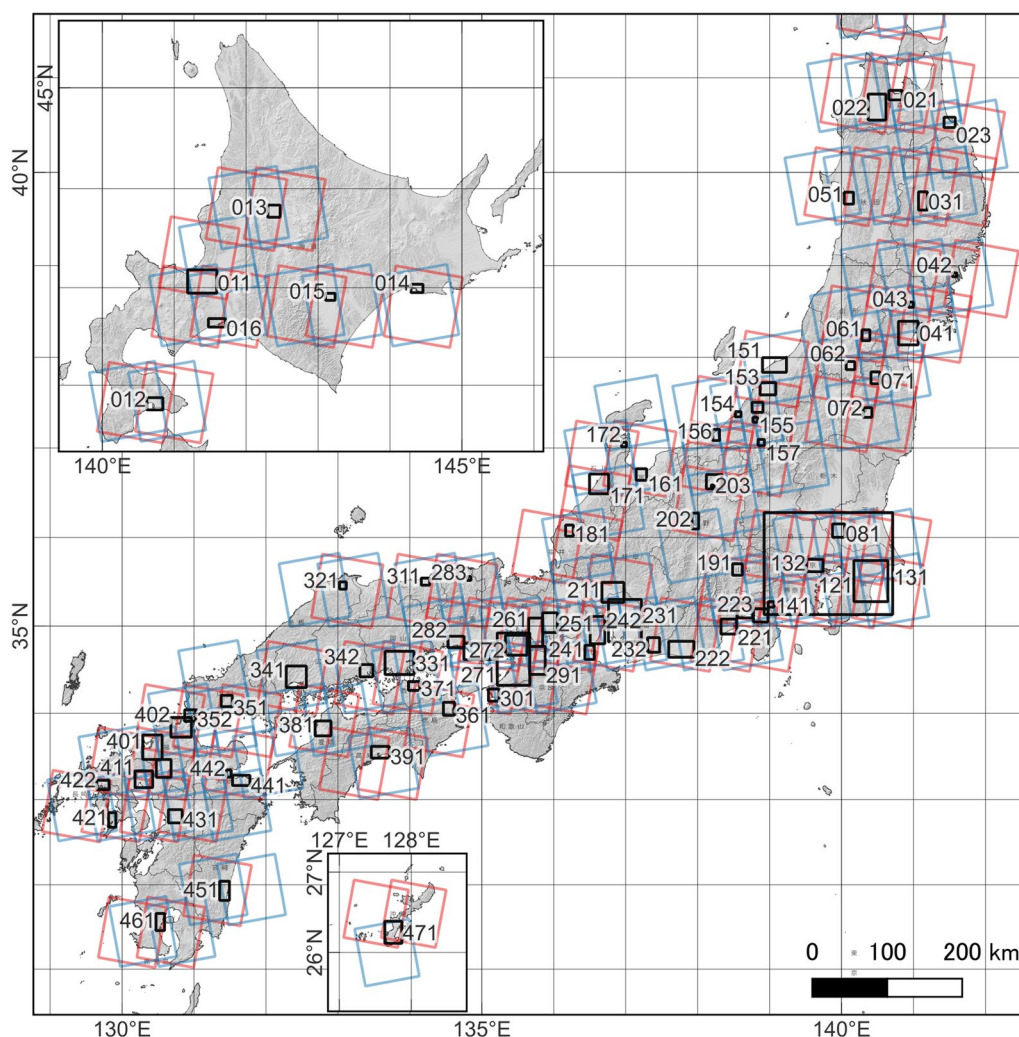
Fig. 1 Footprints of the ALOS frames used in this study. The blue and red rectangles denote the ascending and descending frames, respectively. The black rectangles and three-digit numbers denote the AOI and its ID, respectively (see Table 1)

2.3 Methods

In the previous study using Sentinel-1 data (Morishita 2021), an open-source tool LiCSBAS was used to perform the time series analysis (Morishita et al. 2020). The workflow of LiCSBAS consists of the following 11 steps:

Step 0.1: Download Looking into Continents from Space with Synthetic Aperture Radar (LiCSAR) products

Step 0.2: Convert file format

Step 0.3: Correct tropospheric noise (optional)

Step 0.4: Mask low-coherence regions in the unwrapped interferograms (optional)

Step 0.5: Crop a specified rectangular region of interest (optional)

Step 1.1: Quality check and identification of bad interferograms

Step 1.2: Check loop closure and identify bad interferograms

Step 1.3: Small baseline inversion

Step 1.4: Calculate velocity standard deviations

Step 1.5: Mask time series

Step 1.6: Filter (and deramp) the time series

LiCSBAS is designed to semi-automatically perform time series analysis using Centre for the Observation and Modelling of Earthquakes, Volcanoes and Tectonics (COMET) LiCSAR products derived from Sentinel-1 data (Lazecký et al. 2020). Step 0.1 is dedicated to the download of the LiCSAR products. However, any other InSAR products derived from any SAR satellites can be processed by LiCSBAS from Step 0.2 as long as

Morishita *et al. Progress in Earth and Planetary Science* (2023) 10:66

Page 6 of 20

the required data (i.e., unwrapped data, coherence, and other metadata) are prepared in the predefined format.

To download the AIST ALOS InSAR products and convert them to the LiCSBAS-ready format, a patch tool LiCSBASpatch_AIST_ALOS is available as a replacement for Step 0.1 in LiCSBAS. This patch tool allows us to perform all steps of LiCSBAS for AIST ALOS InSAR products.

In contrast to Sentinel-1, the baseline condition of ALOS data must be carefully considered. Since the orbit of modern space-borne SAR satellites such as Sentinel-1 and ALOS-2 is well controlled, the perpendicular baseline of the interferometric pair is always small and the DEM error component can be ignored in the time series analysis (Morishita et al. 2020; Morishita 2021). However, the baseline of ALOS is much longer than that of modern SAR satellites and also temporally correlated, which would introduce a significant false signal proportional to the DEM error in the displacement time series (Samsonov 2010; Fattahi and Amelung 2013). While LiCSBAS does not have a function to compensate for the DEM error component, this function has been implemented in Step 1.6 in the newly developed LiCSBAS2. The DEM error component, which is proportional to the perpendicular baseline, is estimated and subtracted from the displacement time series after deramping and before the spatiotemporal filtering in Step 1.6. For more details on the effect of DEM error noise reduction, see Sect. 4.2. LiCSBAS2 ver1.9.0-alpha was used in this study. Steps other than Step 1.6 in LiCSBAS2 are the same as in LiCSBAS.

The number of epochs or interferograms for each frame is much smaller (max. 30 epochs) than that of Sentinel-1 (max. 136 epochs) due to the low observing frequency of ALOS (Additional file 1: Table S1). However, the spatial resolution is much higher ($\sim$ 30 m) than that of COMET LiCSAR Sentinel-1 products ($\sim$ 100 m), resulting in $\sim$ 10 times more data for each epoch or interferogram. Consequently, the total amount of data processed is larger than Sentinel-1. In particular, Step 1.3 takes a long time for a large number of pixels, even with parallel processing using multiple Central Processing Units (CPUs). To reduce the processing time, the Graphics Processing Unit (GPU) option implemented in LiCSBAS ver 1.5.0 (March 5, 2021) or later was used. For example, Step 1.3 for frame 405_0702_343 in 131 Kanto (29 epochs, 265 interferograms, image size 3712×3970) took 131 min to complete with 5 CPU cores (resource type of rt_C.small in ABCI), but only 29 min with GPU 16 GB memory (rt_G.small).

In the preprocessing steps of LiCSBAS, the tropospheric noise correction using Generic Atmospheric Correction Online Service (GACOS) data in Step 0.3 was not applied because (1) the target area is flat and therefore the stratified tropospheric noise is minimal; (2) the turbulent noise is significantly mitigated in Step 1.6 by a spatiotemporal filter (Morishita et al. 2020; also see Sect. 4.1). Low coherence pixels were masked in Step 0.4 with an average coherence threshold of 0.2. Unwrapped data were cropped for each AOI in Step 0.5.

To significantly reduce the bad effect of unwrapping errors and to keep only high-coherence interferograms with almost full coverage of unwrapped data, the thresholds of the unwrapped pixel rate in Step 1.1 and the root mean square of the loop phase in Step 1.2 were set to 0.8 and 1.0, respectively, which are stricter than the default values of 0.3 and 1.5, respectively. As a result, most interferograms with long perpendicular baselines were automatically rejected. However, in contrast to C-band Sentinel-1, many interferograms with long temporal baselines and short perpendicular baselines remained due to the slow temporal decorrelation of L-band and urban areas (Morishita and Hanssen 2015). In addition, some interferograms or epochs suffering from severe noise (e.g., due to ionospheric disturbances) were manually removed (Additional file 1: Table S2). The refined interferometric network contained no gaps in all AOIs and frames. The number of remaining interferograms and epochs varies widely from frame to frame, ranging from 10 to 338 and 5 to 30, respectively (Additional file 1: Table S1).

To retain only high-precision pixels, strict masking thresholds were applied, i.e., the number of gaps (n_gap) was set to 0 (i.e., no gaps are allowed), the number of loop errors (n_loop_err) was set to 0 (i.e., no potential unwrapping errors were allowed), and the number of no loop interferograms (n_ifg_noloop) was set to 0 (i.e., all interferograms at all pixels must have at least one loop to check for phase unwrapping errors). Despite these strict parameters, a sufficient number of interferograms and pixels remained due to the low temporal decorrelation characteristic of the L-band (Morishita and Hanssen 2015).

While the ionospheric noise in L-band is intense, the ionospheric noise correction has not been applied to the AIST ALOS InSAR products (Sugimoto et al. 2021). To mitigate the significant ionospheric noise, a deramp in Step 1.6 was necessary. While the ionospheric noise was approximated by a linear ramp for small areas, a quadratic polynomial was used for relatively large AOIs (i.e., 131 Kanto, 152 Nagoya, 271 Osaka). The temporal and spatial filter widths in Step 1.6 were the default values (i.e., three times the average temporal interval and 2 km, respectively, Additional file 1: Table S1). The temporal filter width differs from frame to frame and AOI to AOI, depending on the average temporal interval, and mostly ranges from 170 to 300 days, which is much longer than

that of Sentinel-1 due to the low frequency of ALOS observations. This reduces the ability to detect nonlinear or seasonal deformation signals. See Sect. 4.1 for discussion.

We then computed the velocity for each AOI and frame from the deformation time series. The reference area was set to the whole area (i.e., average of all pixels), while the reference areas to discuss the time series at specific points were selected separately around the points of interest in Sect. 3. We also tried calculating the amplitude and time offset of the seasonal component according to Morishita (2021), but their accuracy was not high enough to discuss the seasonal component

due to the low observation frequency of ALOS. Therefore, we do not discuss the seasonal component in the following sections. After deriving the line-of-sight (LOS) velocity for each AOI and frame, we decomposed the ascending and descending LOS velocities from multiple frames into vertical and east–west (EW) velocities in each AOI (Wright et al. 2004; Morishita 2021).

3 Results and comparison to Sentinel-1
3.1 Overview
Similar to the Sentinel-1 results reported in Morishita (2021), many deformation signals were detected in this study (Table 1). Some AOIs show consistent
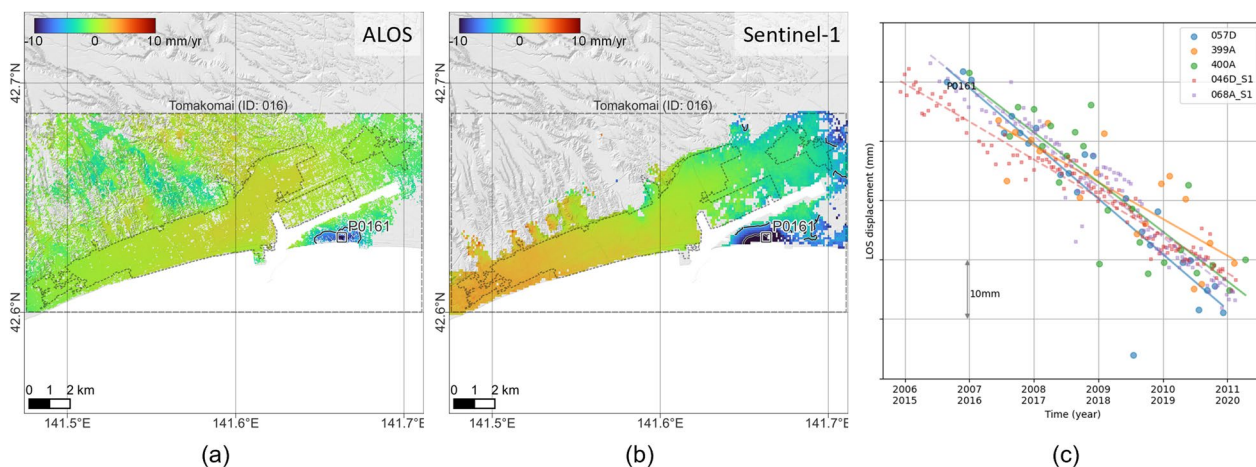
Fig. 2 Deformation in 016 Tomakomai, Hokkaido. **a** and **b** are the vertical deformation velocities derived from ALOS and Sentinel-1, respectively. The black dashed lines are the boundaries of the DID. The black solid lines denote the 5 mm/year contour lines without the 0 mm/year lines. **c** The LOS deformation time series at P0161 derived from ALOS (2006–2011, large circles) and Sentinel-1 (2014–2020, small rectangles) data
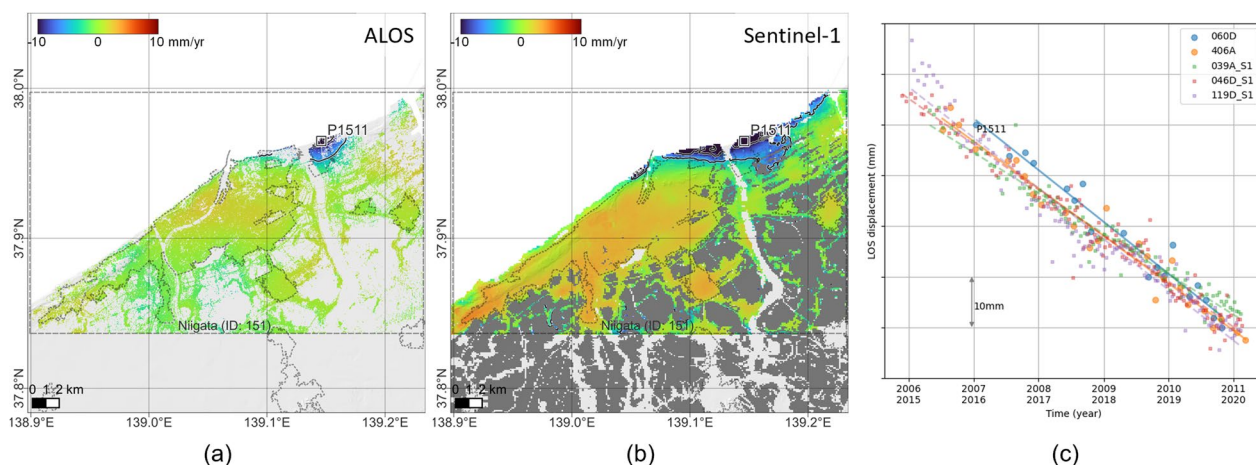

Fig. 3 Deformation in 151 Niigata. **a** and **b** are the vertical deformation velocities derived from ALOS and Sentinel-1, respectively. The black dashed lines are the boundaries of the DID. The black solid lines denote the 5 mm/year contour lines without the 0 mm/year lines. The gray areas in **b** denote the rice paddy fields. **c** The LOS deformation time series at P1511 derived from ALOS (2006–2011, large circles) and Sentinel-1 (2014–2020, small rectangles) data

deformation with Sentinel-1, while others show significantly different deformation signals. For example, linear subsidence was detected in 016 Tomakomai (Fig. 2) and 151 Niigata (Fig. 3), and its rate (∼ 10 mm/year) and spatial extent are consistent with Sentinel-1, suggesting that the subsidence has been constant for more than 15 years. In 022 Hirosaki (Fig. 4), 121 Kujyukuri (Fig. 5), 171 Kanazawa (Fig. 6), and 203 Matsushiro (Fig. 7), significant linear subsidence was detected similar to Sentinel-1, but the spatial and temporal pattern was different. At 081 Joso (Fig. 8), 132 Yoyogi (Fig. 9), 152 Nagoya (Fig. 10), and 261 Kyoto (Fig. 11), uplift or subsidence signals were detected by ALOS, but there were no or much slower deformation signals in the Sentinel-1 result, meaning that these deformations occurred in the past limited period and then stopped or strongly decelerated. While interesting nonlinear deformation was detected by Sentinel-1 at 153 Sanjo

(Additional file 1: Fig. S1), 291 Nara (Additional file 1: Fig. S2), and 431 Kumamoto (Additional file 1: Fig. S3), these areas were very stable in the ALOS period. In the following subsections, we pick up several interesting deformation signals detected by ALOS and compare them with the Sentinel-1 result.

As the target areas are flat plains, significant horizontal deformation is not expected and therefore independent ascending and descending results should show consistent results. In fact, all the ascending and descending results showed consistent deformation and no significant unexpected EW deformation was detected.

In the Sentinel-1 result, most of the rice paddy fields showed subsidence, presumably due to the systematic bias caused by the fading signal (Ansari et al. 2021; Morishita 2021). We have masked the rice paddy fields in the figures of the Sentinel-1 results in the comparison to
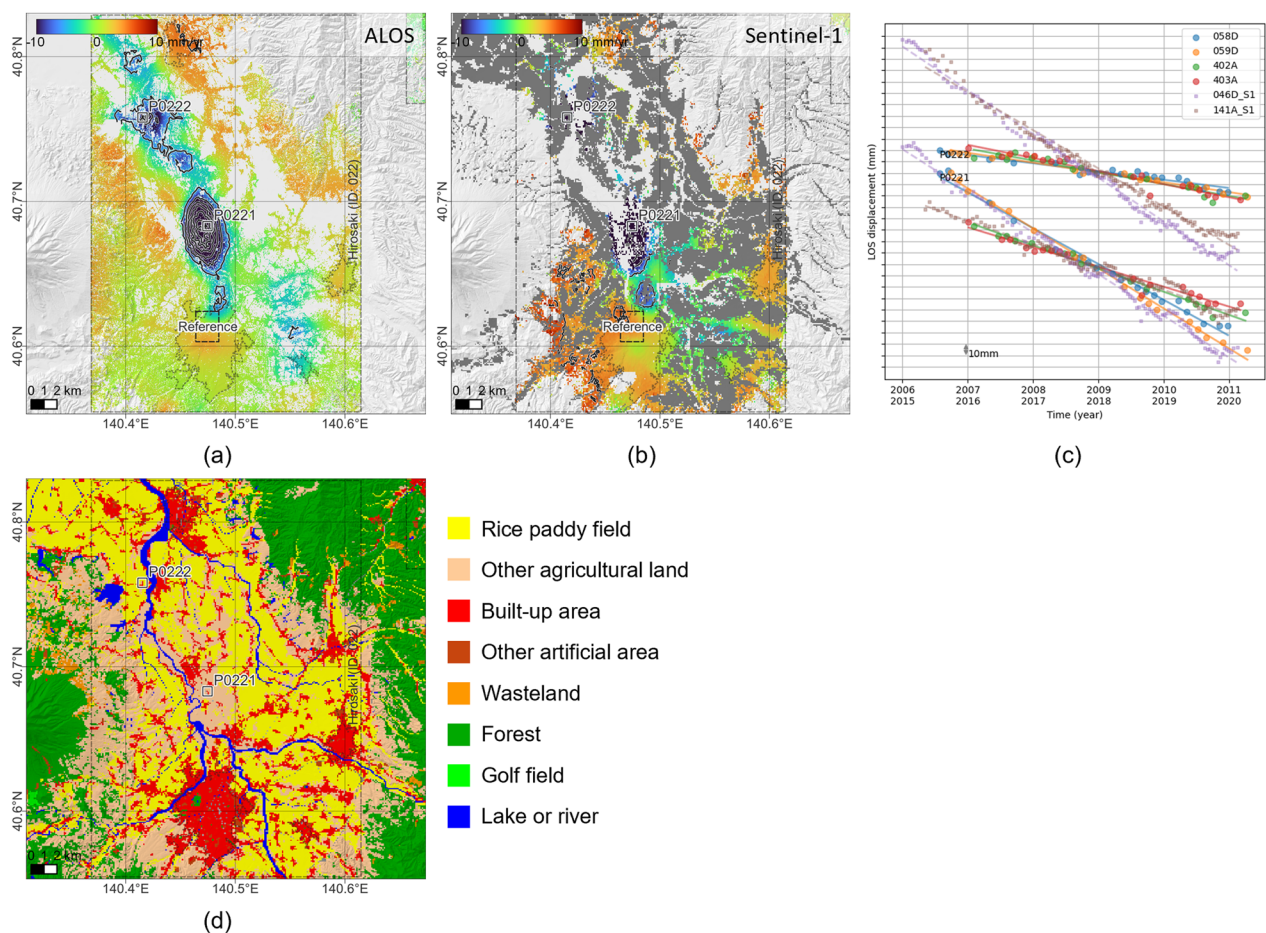

Fig. 4 Deformation in 022 Hirosaki, Aomori. **a** and **b** are the vertical deformation velocities derived from ALOS and Sentinel-1, respectively. The black dashed lines are the boundaries of the DID. The black solid lines denote the 5 mm/year contour lines without the 0 mm/year lines. The gray areas in **b** denote the rice paddy fields. The dashed black rectangles are the reference area for the time series. **c** The LOS deformation time series at P0211 and P0222 derived from ALOS (2006–2011, large circles) and Sentinel-1 (2014–2020, small rectangles) data. **d** The land-use and land-cover map
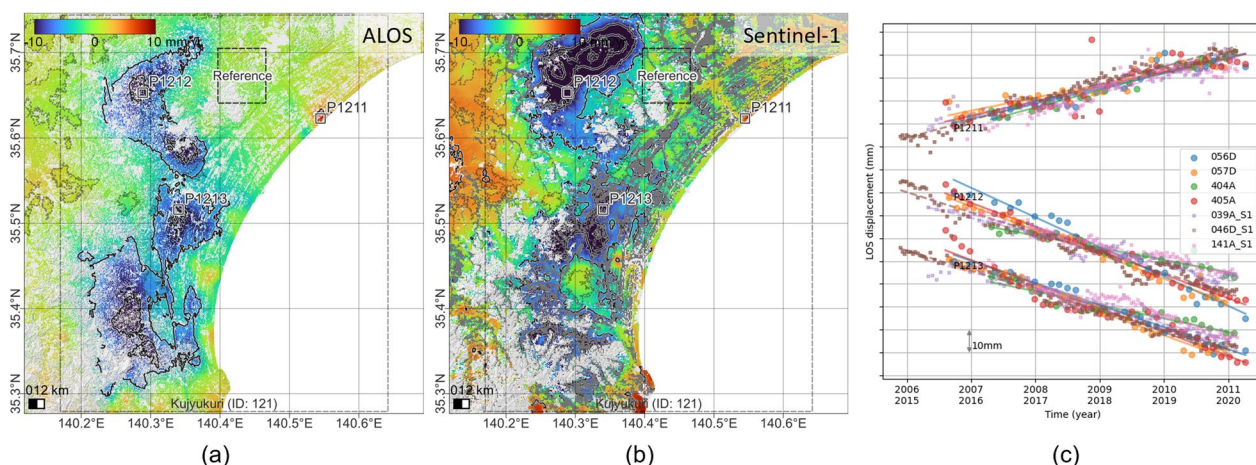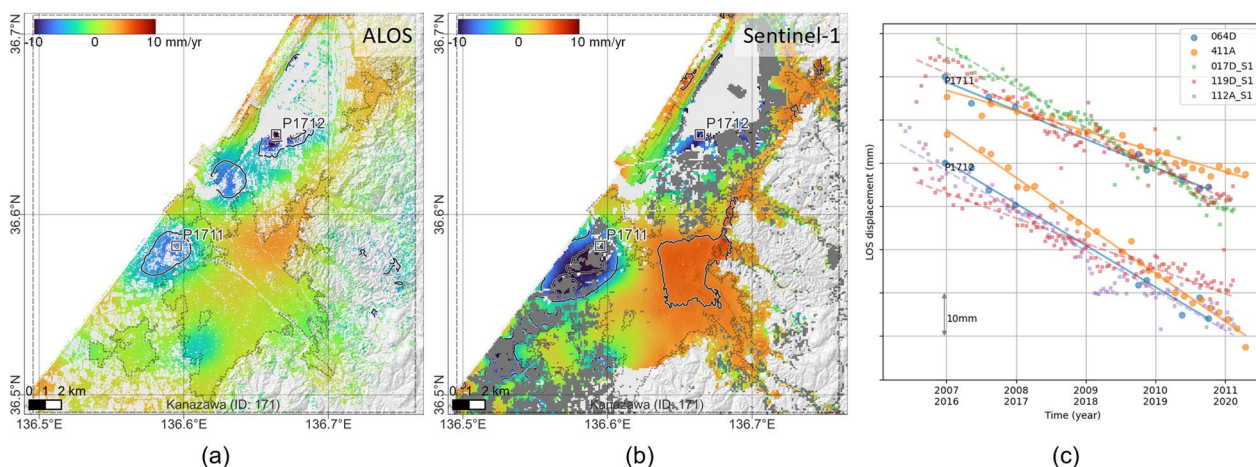
Fig. 5 Deformation in 121 Kujyukuri, Chiba. **a** and **b** are the vertical deformation velocities derived from ALOS and Sentinel-1, respectively. The black dashed lines are the boundaries of the DID. The black solid lines denote the 5 mm/year contour lines without the 0 mm/year lines. The gray areas in **b** denote the rice paddy fields. The dashed black rectangles are the reference area for the time series. **c** The LOS deformation time series at P1211-P1213 derived from ALOS (2006–2011, large circles) and Sentinel-1 (2014–2020, small rectangles) data

Fig. 6 Deformation in 171 Kanazawa, Ishikawa. **a** and **b** are the vertical deformation velocities derived from ALOS and Sentinel-1, respectively. The black dashed lines are the boundaries of the DID. The black solid lines denote the 5 mm/year contour lines without the 0 mm/year lines. The gray areas in **b** denote the rice paddy fields. **c** The LOS deformation time series at P1711 and P1712 derived from ALOS (2006–2011, large circles) and Sentinel-1 (2014–2020, small rectangles) data

hide the possible effect of the systematic bias and to make the comparison easy (also see Sect. 4.3).

When plotting the time series at a specific point in a wide AOI, the region considered stable near that point was redefined as the reference region to reduce the effect of spatially long-wavelength residual errors. (Such cases are explicitly shown in the figure.)

3.2 Subsidence
3.2.1 022 Hirosaki, Aomori
Rapid subsidence (max. ~40 mm/year) in two separate regions was detected in 022 Hirosaki (Fig. 4). Although

Sentinel-1 also detected the two subsidence signals and the velocity in the southern region (P0221) is almost the same, the velocity in the northern region (P0222) of ALOS is significantly slower (~10 mm/year) than that of Sentinel-1 (~40 mm/year). In terms of point coverage, ALOS has much better coverage than Sentinel-1, especially in orchard areas, while no points were obtained in rice paddy fields, even with ALOS, due to the drastic change in surface conditions (i.e., filled with water in spring and dried in winter). This better coverage of ALOS allows us to know the spatial extent of subsidence and to detect unknown subsidence between two major subsidence basins.
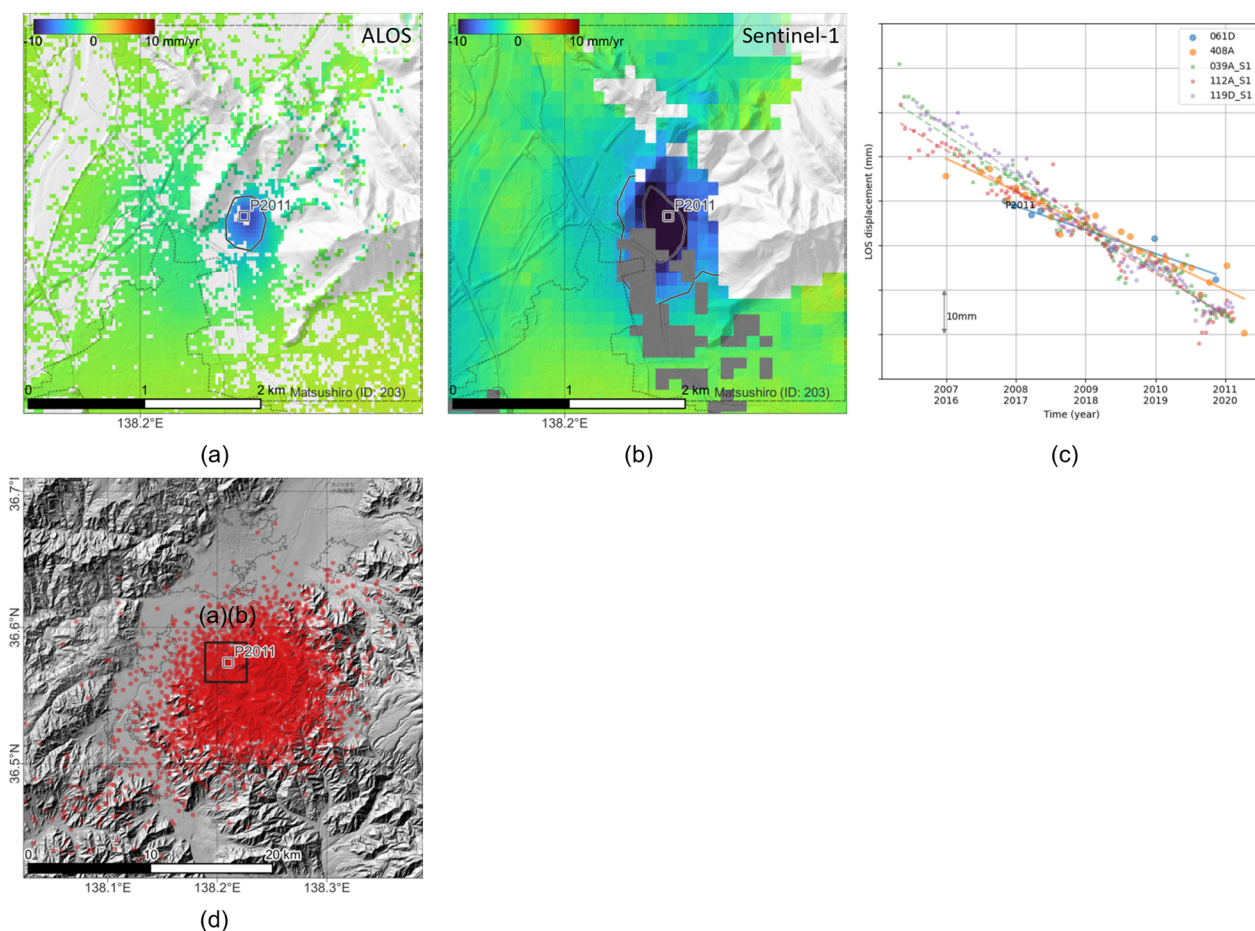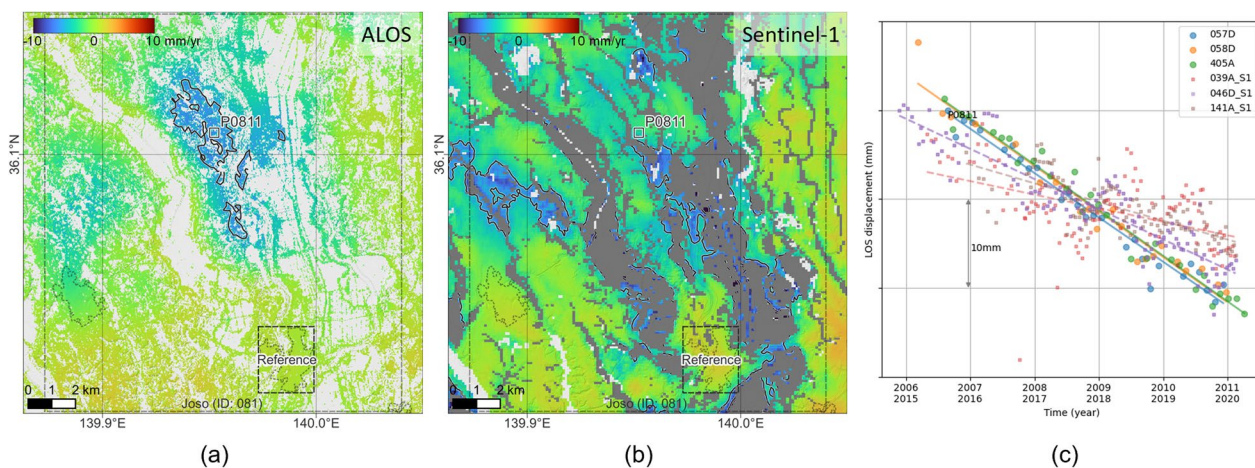
Fig. 7 Deformation in 203 Matsushiro, Nagano. **a** and **b** are the vertical deformation velocities derived from ALOS and Sentinel-1, respectively. The black dashed lines are the boundaries of the DID. The black solid lines denote the 5 mm/year contour lines without the 0 mm/year lines. The gray areas in **b** denote the rice paddy fields. **c** The LOS deformation time series at P2011 derived from ALOS (2006–2011, large circles) and Sentinel-1 (2014–2020, small rectangles) data. **d** The Matsushiro earthquake swarm area. The red dots indicate the epicenters from August 1965 to May 1967

Fig. 8 Deformation in 081 Joso, Ibaraki. **a** and **b** are the vertical deformation velocities derived from ALOS and Sentinel-1, respectively. The black dashed lines are the boundaries of the DID. The black solid lines denote the 5 mm/year contour lines without the 0 mm/year lines. The gray areas in **b** denote the rice paddy fields. The dashed black rectangles are the reference area for the time series. **c** The LOS deformation time series at P0811 derived from ALOS (2006–2011, large circles) and Sentinel-1 (2014–2020, small rectangles) data
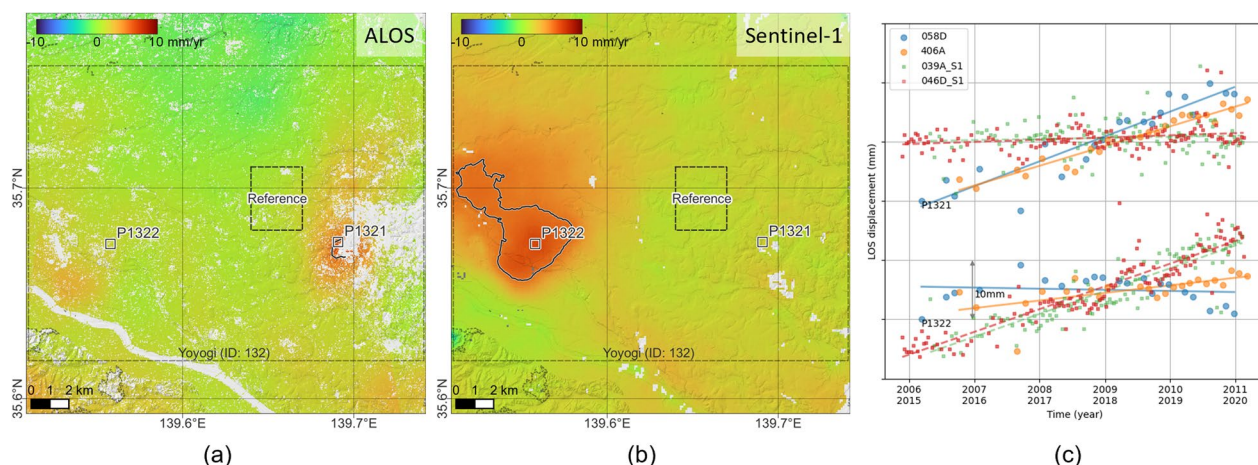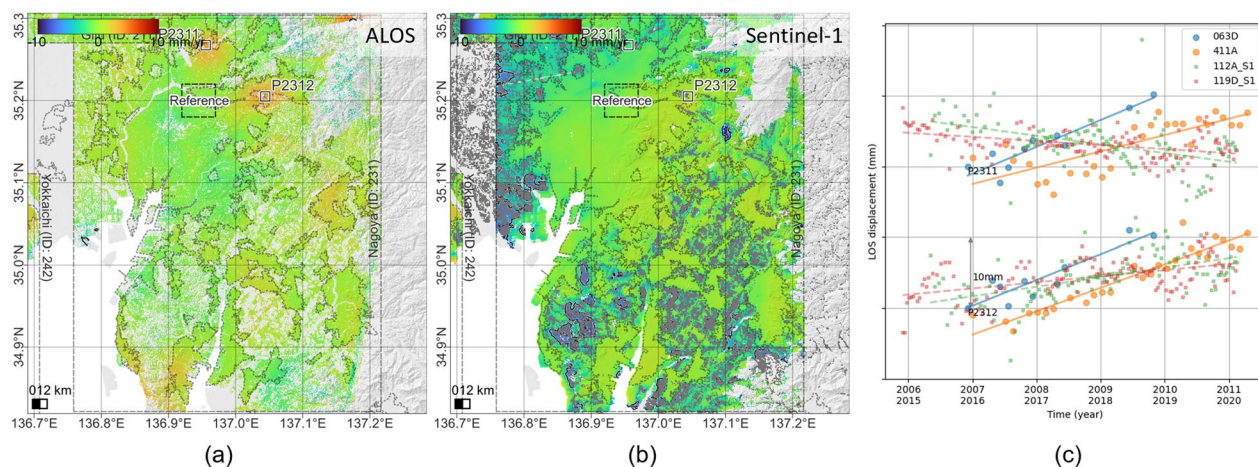
Fig. 9 Deformation in 132 Yoyogi, Tokyo. **a** and **b** are the vertical deformation velocities derived from ALOS and Sentinel-1, respectively. The black dashed lines are the boundaries of the DID. The black solid lines denote the 5 mm/year contour lines without the 0 mm/year lines. The dashed black rectangles are the reference area for the time series. **c** The LOS deformation time series at P1321 and P1322 derived from ALOS (2006–2011, large circles) and Sentinel-1 (2014–2020, small rectangles) data

Fig. 10 Deformation in 231 Nagoya, Aichi. **a** and **b** are the vertical deformation velocities derived from ALOS and Sentinel-1, respectively. The black dashed lines are the boundaries of the DID. The black solid lines denote the 5 mm/year contour lines without the 0 mm/year lines. The gray areas in **b** denote the rice paddy fields. The dashed black rectangles are the reference area for the time series. **c** The LOS deformation time series at P2311 and P2312 derived from ALOS (2006–2011, large circles) and Sentinel-1 (2014–2020, small rectangles) data

3.2.2 121 Kujyukuri, Chiba

The Kujyukuri Plain is one of the largest subsidence areas in Japan. This area is rich in natural gas dissolved in water and has been experiencing subsidence due to natural gas extraction since the 1960s (Shen et al. 2004; Nonaka et al. 2020). Since the 1970s, restrictions on natural gas extraction have been applied to prevent rapid subsidence, but widespread subsidence continues, and even in the 2020s, subsidence of up to about 2 cm/year has been observed by leveling and InSAR time series analysis using Sentinel-1 and ALOS-2 data (Chiba Prefecture 2022; Ishitsuka and Matsuoka 2016; Nonaka et al. 2020; Morishita 2021).

In this study, four ALOS frames are available (i.e., two ascending and two descending; Fig. 1 and Additional file 1: Table S1). The small common reference area among the four frames was set to the northeast of the subsidence area, rather than using the entire area for each frame as a reference to compare the time series from different frames.
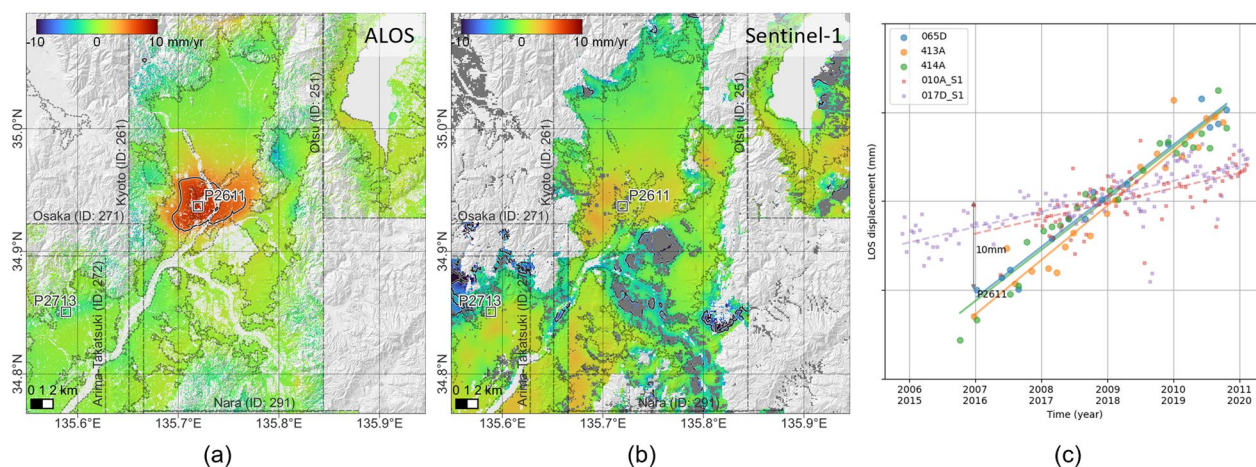
Fig. 11 Deformation in 261 Kyoto. **a** and **b** are the vertical deformation velocities derived from ALOS and Sentinel-1, respectively. The black dashed lines are the boundaries of the DID. The black solid lines denote the 5 mm/year contour lines without the 0 mm/year lines. The gray areas in **b** denote the rice paddy fields. **c** The LOS deformation time series at P2611 derived from ALOS (2006–2011, large circles) and Sentinel-1 (2014–2020, small rectangles) data

The result shows three or four distinct areas of subsidence (Fig. 5). The time series show a nearly linear trend. Although the rough distribution is similar to the Sentinel-1 result, the peak locations and velocities are significantly different. The northern subsidence area around P1212 has been extended to the northeast, and the maximum subsidence rate has been increased from 2006–2011 to 2014–2020. In contrast, the subsidence velocity in the next southern area (between P1212 and P1213) is greater in 2006–2011 than in 2014–2020. Around P1213, there was a single peak of subsidence in 2006–2011, but two new peaks seem to have appeared to the north and west in 2014–2020. Interesting uplift has also been detected in the east of the plain along the coast (P1211, ~5 mm/year) by both ALOS and Sentinel-1, suggesting that this uplift has been going on for more than 15 years with a constant velocity, although the mechanism is unknown.

3.2.3 171 Kanazawa, Ishikawa
Significant subsidence (~10 mm/year) was detected in 171 Kanazawa, as in the case of Sentinel-1 (Fig. 6). There are two distinct areas of subsidence in the north and south. While the northern subsidence around P1712 is almost similar between 2006–2011 and 2014–2020, the southern one around P1711 is faster in 2014–2020 than in 2006–2011, implying that the subsidence has been accelerated. The time series shows almost constant subsidence. The other peak (~5 mm/year) of subsidence was also detected between the two areas in the ALOS result, although it is not clear in the Sentinel-1 result.

3.2.4 203 Matsushiro, Nagano
Very localized subsidence (~500 m diameter, ~5 mm/year) was detected at 203 Matsushiro, Nagano (Fig. 7). The larger and faster subsidence (~1 km, 10 mm/year) was also detected by Sentinel-1 in the later period at the same location, suggesting that the subsidence has continued and gradually accelerated for at least more than 13 years.

The Matsushiro earthquake swarm started in August 1965, and the subsidence area detected by this study is located on the northwest side of the earthquake swarm area with a diameter of ~15 km (Fig. 7d; Japan Meteorological Agency 2016). Groundwater and hot springs were gushed out in association with this earthquake swarm, and the earthquake swarm is thought to have been caused by the intrusion of deep groundwater into the focal area (Okusawa and Tsukahara 2001). The largest earthquake of M5.4 occurred on April 5, 1966, and the peak of seismic activity was around that time. The total number of earthquakes until the end of 1966 was >600 thousand. While the number of earthquakes has decreased significantly since then, seismic activity is still being observed. More than 90 cm of localized uplift in September 1966 and exponential subsidence thereafter were detected by leveling around the recent subsidence area (Okada and Tsubokawa 1970). The recent subsidence detected by this study may also be related to the past earthquake swarm and groundwater activity.

3.2.5 081 Joso, Ibaraki
ALOS detected slow subsidence (~5 mm/year) outside the DID at 081 Joso, Ibaraki, while the Sentinel-1 result

shows no clear subsidence there (Fig. 8). A consistent subsidence signal was also detected by the stacking approach using ALOS data (Yamanaka et al. 2013).

3.3 Uplift
3.3.1 132 Yoyogi, Tokyo
A slow uplift signal (~ 5 mm/year) was detected at 132 Yoyogi, Tokyo (Fig. 9a). Although it is difficult to discuss the nonlinearity of the time series from these infrequent temporal sampling observations, the uplift appears to have occurred or accelerated in 2008 and 2009 (Fig. 9c). There does not seem to be a clear temporal correlation with the groundwater level change (Tokyo Metropolitan Government 2022).

While the Sentinel-1 result shows no uplift at Yoyogi, a different uplift signal was detected at Chofu, 10–15 km west of Yoyogi (Morishita 2021). Interestingly, the uplift area shifted from Yoyogi to Chofu in about 10 years, although the relationship between the two uplifts is unknown.

3.3.2 152 Nagoya, Aichi
Although no significant deformation (> 5 mm/year) was detected in 152 Nagoya, slow uplift (~ 4 mm/year) was detected in two northern areas; P2311 Kasugai City and P2312 Owariasahi City (Fig. 10). These uplift signals were not detected in the Sentinel-1 result. The time series show different features; an episodic uplift around P2311 might have occurred in the first half of 2009, while the uplift around P2312 seems to be almost constant, though the temporal characteristics are not very clear from the infrequent observations.

3.3.3 261 Kyoto
Significant uplift with almost constant velocity (> 5 mm/year) was detected in 261 Kyoto (Fig. 11). The constant uplift in almost the same area is also seen in the Sentinel-1 result, but the velocity is lower (~ 3 mm/year) than in the ALOS result. Hashimoto (2016) also reported the consistent uplift signal, discussed the onset of the uplift using older European Remote-Sensing Satellite (ERS) and Environmental Satellite (Envisat) data, and concluded that the uplift may have started around 2003–2004 and was caused by the recovery of the groundwater table.

3.4 Tectonic-related deformation
3.4.1 154 Kashiwazaki, Niigata
The Mw 6.6 Niigata-ken Chuetsu-oki earthquake occurred on July 16, 2007. The epicenter was located ~ 20 km north-northeast of Kashiwazaki. The earthquake caused widespread large deformation around the epicenter due to the reverse fault slip of the main seismogenic fault (Aoki et al. 2008; Nishimura et al. 2008b).

In addition, the episodic growth of active folds 15 km east of the epicenter was also detected by ALOS InSAR (Nishimura et al. 2008a). The deformation in Kashiwazaki was not given much attention at that time, but the coseismic interferograms clearly show some phase changes that may represent linear surface ruptures along the subsidiary faults, as seen in the 2016 Kumamoto earthquake (Fujiwara et al. 2016, 2020) (Fig. 12d, e).

In this study, we derived the time series after the earthquake to detect the postseismic deformation. The velocity shows two subsidence regions with linear boundaries (Fig. 12a). The spatial pattern shows some consistency with the coseismic deformation. In particular, the linear feature with an EW direction (around the middle between P1541 and P1542) corresponds to the small hill line with < 10 m relative height (Fig. 12f), which may be an unknown subsidiary fault. The time series shows a rapid exponential decay just after the earthquake (Fig. 12c). P1541 shows ~ 2 cm subsidence between July 19 and October 19, 2007, and then almost constant slow subsidence of ~ 5 mm/year after 2008. Similar exponential decay was also observed around the Kumamoto subsidiary faults after the 2016 Kumamoto earthquake (Morishita 2021).

Interestingly, the Sentinel-1 result shows small subsidence (~ 3 mm/year) in almost the same area (Fig. 12b). The time series shows that the subsidence is not constant, but episodic in February 2018 (Fig. 12c). At the same time, episodic subsidence was observed in Sanjo, ~ 50 km northeast of Kashiwazaki, probably due to unusually heavy snowfall and associated overpumping of groundwater (Morishita et al. 2020; Morishita 2021). Considering the geographical situation, the cause of episodic subsidence in Kashiwazaki is probably the same as that in Sanjo. This implies that the subsidiary faults have controlled the spatial extent of subsidence associated with groundwater change.

3.4.2 272 Arima-Takatsuki, Osaka
Hashimoto (2016) detected the transition of the deformation around the Arima-Takatsuki fault zone using ERS, Envisat, and ALOS from 1992 to 2010. In this study, consistent deformation was detected as expected (Fig. 13). Morishita (2021) revealed the further change of the deformation style in the later period by Sentinel-1. For a more detailed discussion, please refer to Hashimoto (2016) and Morishita (2021).

3.4.3 141 Mt. Hakone, Kanagawa
A significant subsidence signal was detected at Mt. Hakone (Fig. 14), although it is outside the scope of this study (i.e., non-urban area). Sentinel-1 was unable to obtain any measurement points in this area due to
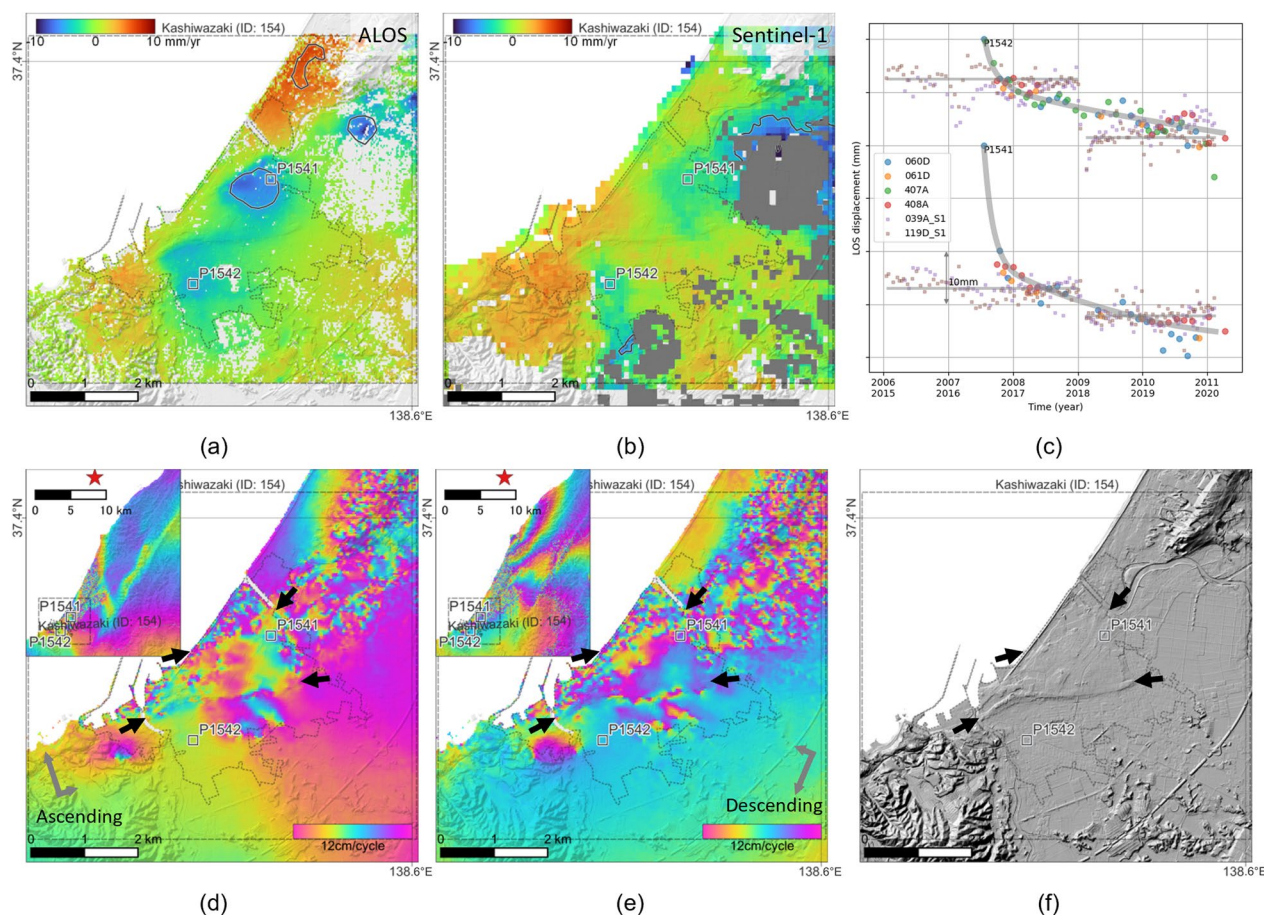
Fig. 12 Deformation in 154 Kashiwazaki, Niigata. **a** and **b** are the vertical deformation velocities derived from ALOS and Sentinel-1, respectively. The black dashed lines are the boundaries of the DID. The black solid lines denote the 5 mm/year contour lines without the 0 mm/year lines. The gray areas in **b** denote the rice paddy fields. **c** The LOS deformation time series at P1541 and P1542 derived from ALOS (2006–2011, large circles) and Sentinel-1 (2014–2020, small rectangles) data. **d** and **e** are the coseismic interferograms associated with the Mw 6.6 Niigata-ken Chuetsu-oki earthquake on July 16, 2007, in the ascending (June 14–July 30, 2007) and descending (January 16–July 19, 2007) orbits, respectively. The black arrows indicate the locations of the edges of the subsidiary faults. The insets show the wider area containing the broad coseismic deformation and the red stars denote the epicenter of the earthquake. **f** The hill shade map

decorrelation. This example clearly shows the strong capability of the L-band to detect deformation in non-urban areas.

A small phreatic eruption occurred in 2015 (Doke et al. 2018; Kobayashi et al. 2018), and the subsidence detected here occurred close to the eruption area. Doke et al. (2020) also detected consistent subsidence signals using ALOS data and suggested that the subsidence is related to the decreased supply of hydrothermal fluids from deeper areas. For a more detailed discussion, see Doke et al. (2020).

4 Discussion
4.1 Advantages and disadvantages over Sentinel-1
In general, ALOS results have better coverage than Sentinel-1, especially in vegetated areas (see Sects. 3.2.1 and 3.4.3). One of the main reasons is the slower temporal

decorrelation of the L-band (Morishita and Hanssen 2015). In addition, the ease of phase unwrapping in the L-band is also an important factor. Since LiCSBAS rejects interferograms with many unwrapping errors in Step 1.2 and pixels with possible unwrapping errors in Step 1.5, the success rate of the phase unwrapping has an impact on the coverage. A phase difference of one-quarter of the wavelength (i.e., half cycle or π rad; ~ 6 cm in L-band and 1.4 cm in C-band) can cause a phase unwrapping error (e.g., Chen and Zebker 2002). In C-band, a few centimeters of atmospheric noise can cause a phase unwrapping error between separated regions, while in L-band this risk is much lower.

However, there is a critical drawback to ALOS, the low temporal frequency of the observations. In most frames, the observation frequency is 3–6 times/year (Additional file 1: Table S1), while that of Sentinel-1 is 30–60
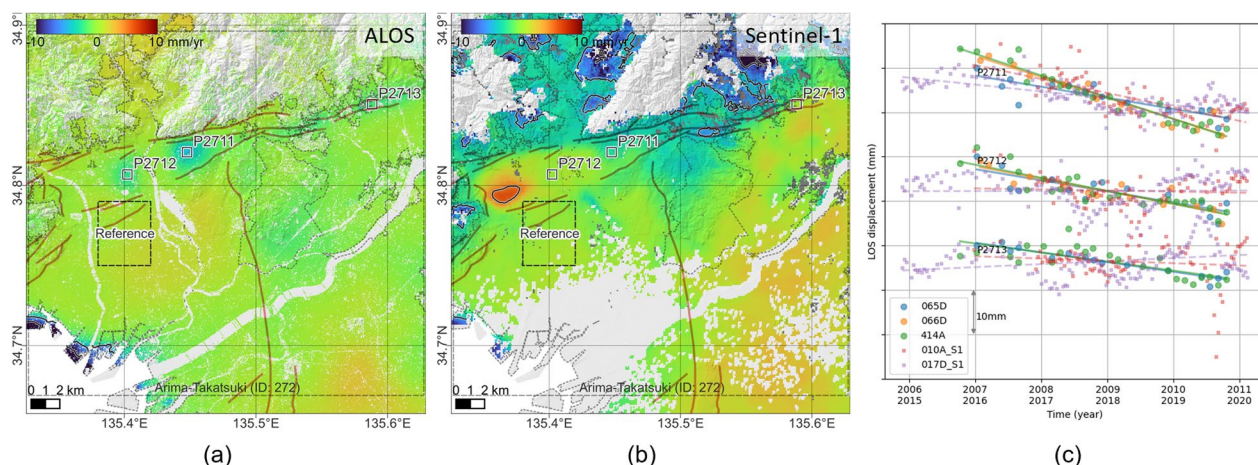
Fig. 13 Deformation in 272 Arima-Takatsuki, Osaka. **a** and **b** are the vertical deformation velocities derived from ALOS and Sentinel-1, respectively. The black dashed lines are the boundaries of the DID. The black solid lines denote the 5 mm/year contour lines without the 0 mm/year lines. The gray areas in **b** denote the rice paddy fields. The red lines denote the known active faults. The dashed black rectangles are the reference area for the time series. **c** The LOS deformation time series at P2711-P2713 derived from ALOS (2006–2011, large circles) and Sentinel-1 (2014–2020, small rectangles) data
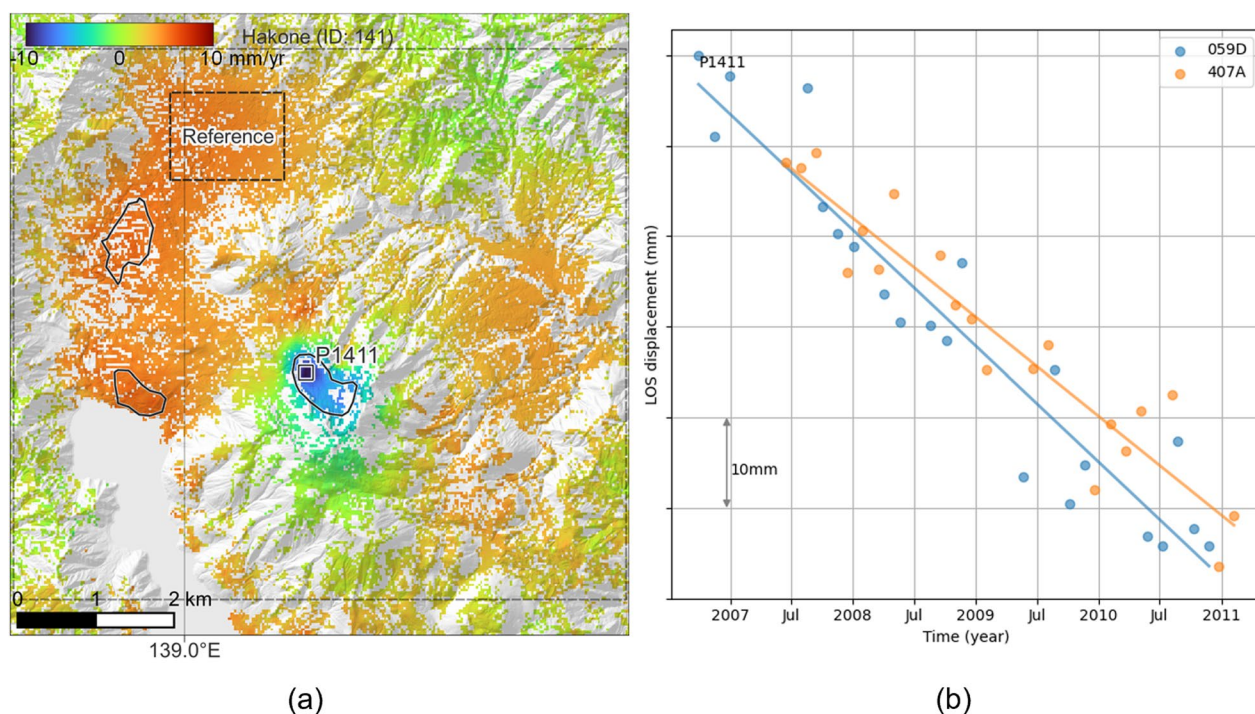

Fig. 14 Deformation in 141 Mt. Hakone, Kanagawa. **a** The vertical deformation velocities derived from ALOS. The black solid lines denote the 5 mm/ year contour lines without the 0 mm/year lines. The dashed black rectangle is the reference area for the time series. **b** The LOS deformation time series at P1411 derived from ALOS data

times/year. It is almost impossible to capture the details of seasonal or nonlinear deformation time series. For example, in 155 Ojiya, Niigata, large seasonal deformation (i.e., > 5 cm sudden subsidence in winter caused by groundwater pumping, followed by gradual recovery) was detected by Sentinel-1 (Morishita et al. 2020; Morishita 2021). In contrast, it is quite difficult to find out the seasonal deformation from the ALOS time series with only 3–6 times/year, although the limited time series data are consistent with the seasonal deformation (Fig. 15).
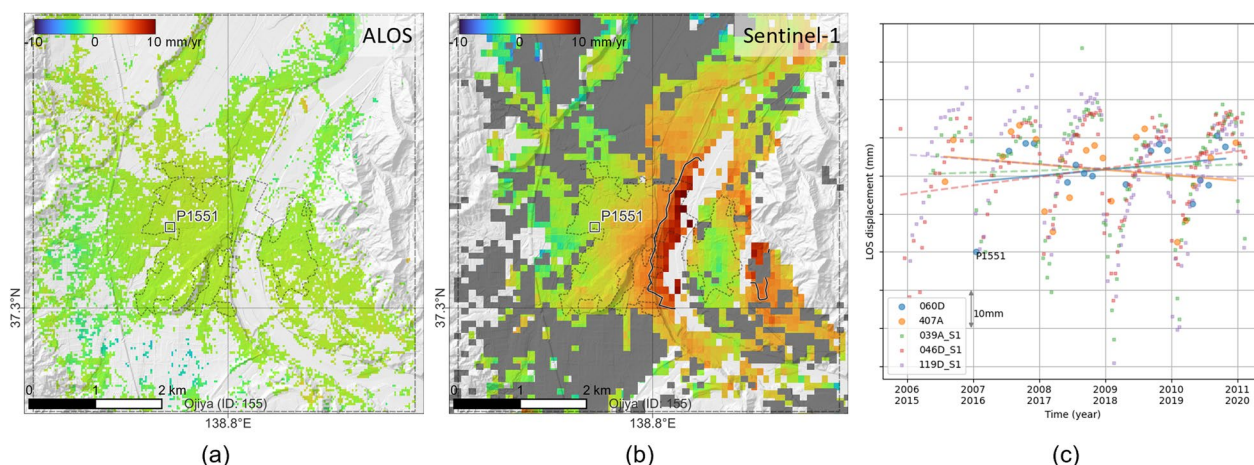
Fig. 15 Deformation in 155 Ojiya, Niigata. **a** and **b** are the vertical deformation velocities derived from ALOS and Sentinel-1, respectively. The black dashed lines are the boundaries of the DID. The black solid lines denote the 5 mm/year contour lines without the 0 mm/year lines. The gray areas in **b** denote the rice paddy fields. **c** The LOS deformation time series at P1551 derived from ALOS (2006–2011, large circles) and Sentinel-1 (2014–2020, small rectangles) data

In addition, spatially correlated nonlinear deformation is more difficult to distinguish from atmospheric noise. In Step 1.6 of LiCSBAS, the atmospheric noise is estimated and subtracted from the time series by a spatiotemporal filter under the assumption that the atmospheric noise is spatially correlated but temporally uncorrelated (Morishita et al. 2020). The temporal filter width must be sufficiently larger than the observation frequency; otherwise, there will be no effect of the temporal filter. By default, the triple mean temporal interval is used. In the case of ALOS, the temporal filter width is usually 200–400 days, which means that deformation signals shorter than half a year with some spatial correlation are considered atmospheric noise and cannot be detected. On the other hand, Sentinel-1 used a temporal filter width of 55 days, which allowed the clear detection of the seasonal deformation signal (Morishita 2021).

Unfortunately, ALOS-2, launched in 2014 as the successor of ALOS, has a similar low frequency of observations as ALOS, and we have almost no chance to detect the detailed seasonal deformation using L-band data so far (Morishita 2021). However, the next-generation L-band SAR satellites, such as ALOS-4 and NASA-ISRO SAR (NISAR), will have much higher observation frequency than ALOS and ALOS-2 and will enable us to detect the temporally detailed deformation time series with high coverage even in vegetated areas (Jet Propulsion Laboratory 2020; Motohka et al. 2020).

4.2 Effect of DEM error

Unlike modern SAR satellites such as Sentinel-1 and ALOS-2, the perpendicular baseline of ALOS had not been kept as short as possible, resulting in significant DEM error phases as mentioned in Sect. 2.3. The DEM error component can be described by

$$d = -\frac{B_\perp}{r \sin \theta} dh$$

where $B_\perp$ is the perpendicular baseline, r is the slant range distance between the satellite and ground, θ is the look angle, and dh is the DEM error (Fattahi and Amelung 2013). For example, in frame 422_0650_343 at 411 Oita, the perpendicular baseline ranges from about -2000 m to 2000 m with reference to the single prime image. Regarding the DEM error, Tachikawa et al. (2011) reported that the ASTER GDEM version 2 used for the ALOS InSAR products has an average standard deviation of 12.6 m compared to the Geospatial Information Authority of Japan (GSI) 10 m DEM. Assuming the typical ALOS parameters (i.e., $r = 860$ km and $\theta = 34.3°$), $B_\perp = 2000$ m and $dh = 10$ m correspond to ~2 cm error in the displacement.

While the displacement time series without DEM error correction shows a clear correlation with $B_\perp$, most of the fluctuations are removed by the DEM error correction, i.e., most of the displacement component without DEM error correction is due to the DEM error component (Fig. 16c). The significant DEM error component also affects the velocity because $B_\perp$ is correlated with time (Fig. 16a, b). The amplitude of the estimated DEM error is mostly within 5 m, but sometimes exceeds 10 m, which is roughly consistent with the accuracy of the DEM (Fig. 16d). The spatial pattern of the estimated DEM error is roughly correlated with topography (i.e., highlands
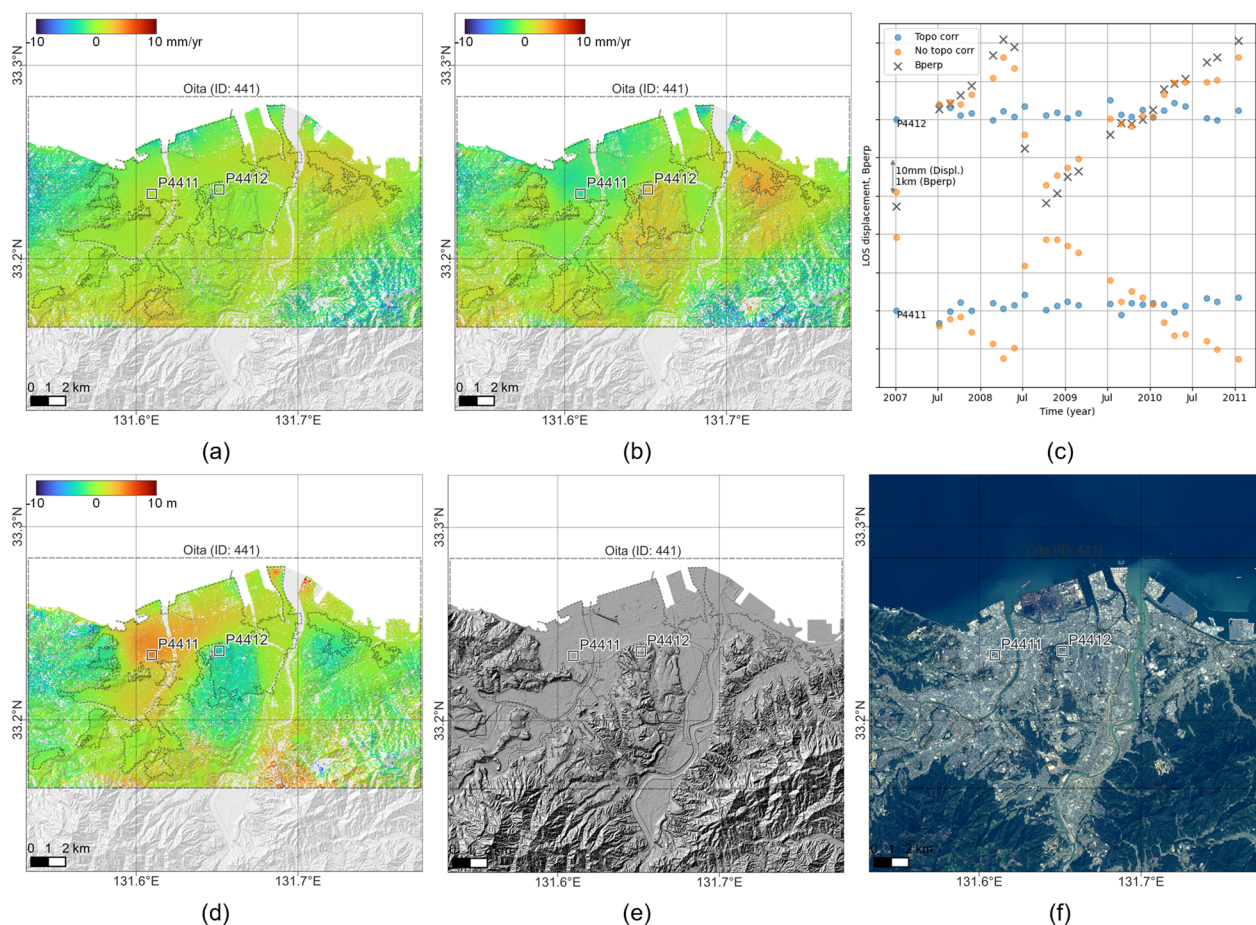
Fig. 16 DEM error effects in 441 Oita. **a** and **b** are the vertical deformation velocities derived from ALOS with and without the DEM error correction, respectively. The black dashed lines are the boundaries of the DID. **c** The LOS deformation time series at P4411 and P4412 derived from ALOS data with and without the DEM error correction and the perpendicular baselines. **d** The estimated DEM error component. **e** The hill shade map. **f** The optical image

tend to have negative DEM error; Fig. 16d, e, f). In addition, in the flat areas, districts with tall buildings tend to have positive DEM errors. This is because many of the actual scatterers are located in high places (e.g., the roof or wall of the buildings), while the DEM does not reflect the height of the buildings.

4.3 Effect of systematic bias due to fading signal

In the Sentinel-1 result, most rice paddy fields showed subsidence signals (Fig. 17c; Morishita 2021). These are presumably not true deformations, but systematic biases due to the fading signal that occurs with multilooked distributed scatterers when only the short time interval interferometric pairs are used in the time series analysis (Ansari et al. 2021). However, in contrast to the Sentinel-1 result, almost no measurement points were obtained on the rice paddy fields in the ALOS result, while L-band can generally maintain high coherence on vegetated areas (e.g., Fig. 17a, d). This is probably due

to the application of large multilook factors and strong filters in the LiCSAR products used to derive the Sentinel-1 result, which produced artificially coherent signals on the rice fields. The ALOS result (i.e., no point in the rice fields) is more natural because the seasonal changes in surface conditions there are too drastic to maintain coherence.

In other non-urban areas, the ALOS result also shows no signal like the systematic bias, while the effect of the fading signal is expected to be greater in the L-band than in the C-band (De Zan et al. 2015). To investigate the effect of the systematic bias, we performed the LiCS-BAS analysis using the ALOS dataset with a bandwidth (i.e., the number of shortest temporal baseline interferograms per epoch; Ansari et al. 2021) of two (bw=2) in the frames covering 081 Joso (i.e., 057_2902_343 and 405_0702_343). The ALOS vertical velocity with bw=2 shows a similar displacement pattern (i.e., subsidence around the rice fields) to the Sentinel-1 result with bw=3
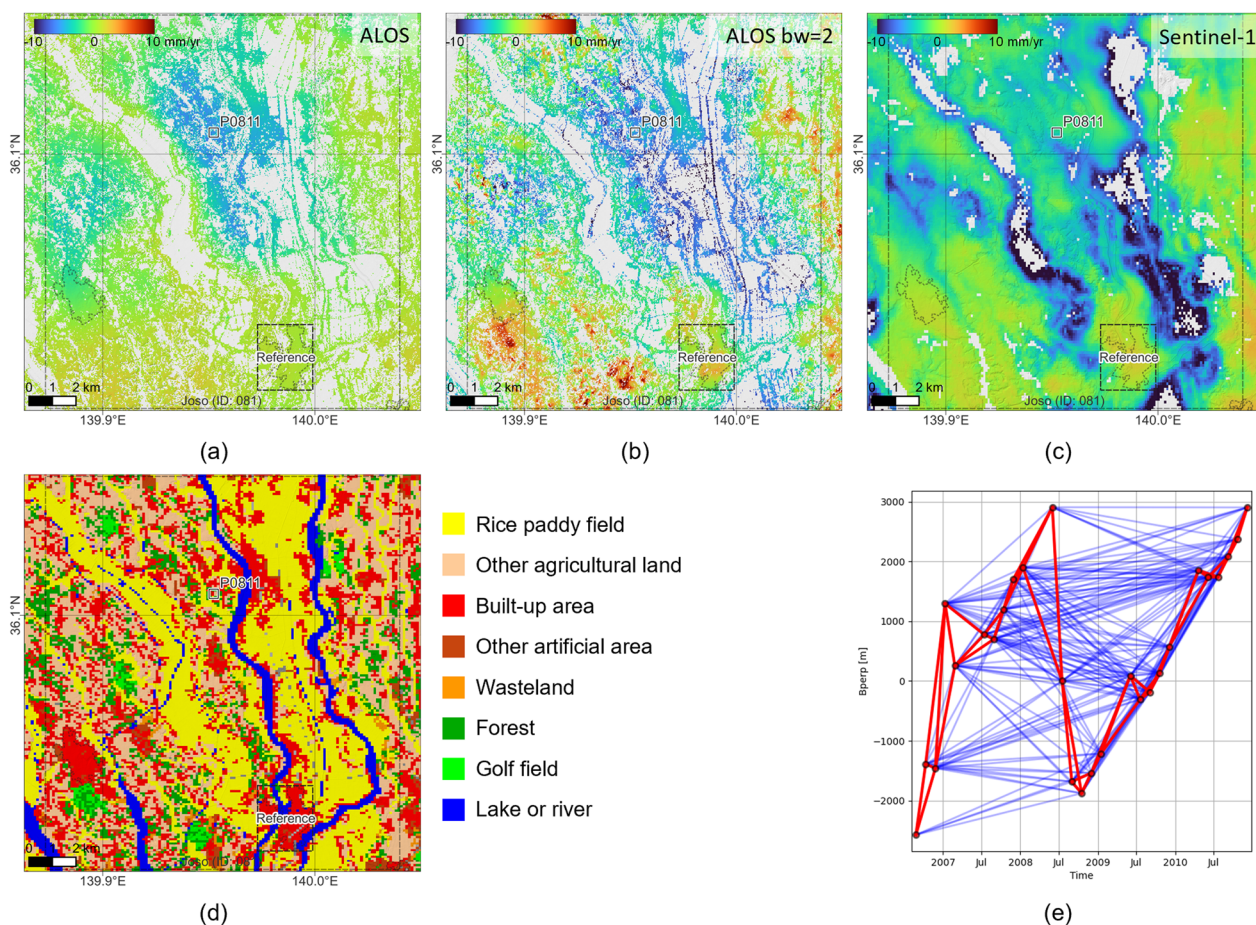
Fig. 17 Effect of the systematic bias in 081 Joso, Ibaraki. **a**, **b**, and **c** are the vertical deformation velocities derived from ALOS with the full bandwidth, ALOS with the bandwidth of two, and Sentinel-1, respectively. The black dashed lines are the boundaries of the DID. The dashed black rectangles are the reference area for the time series. **d** The land-use and land-cover map. **e** The interferometric network with the full bandwidth (blue) and bandwidth of two (red)

or 4 (Fig. 17b, c). Interestingly, significant uplift signals appeared in the ALOS result with bw=2 commonly in the golf fields, which could also be caused by the effect of the systematic bias with the opposite sign to the rice paddy field. While the shortest time interval of ALOS is 46 days, much longer than that of Sentinel-1, the significant systematic bias was generated using only the relatively short-interval interferograms. Therefore, the reason why the ALOS result in this study does not show a systematic bias is probably because this study used not only short-interval but also long-interval interferograms (Fig. 17e). The use of the long-interval interferograms was possible because of the high coherence (i.e., slow temporal decorrelation) of the L-band (Morishita and Hanssen 2015).

The number of available ALOS or ALOS-2 data is not very large due to their infrequent observations (~30 acquisitions for 5 years at most) in contrast to Sentinel-1 (>100 for 5 years). Generating all possible interferograms

as in this study for ALOS or ALOS-2 should not be infeasibly burdensome, and the long-interval interferogram, which can maintain sufficient coherence, would play a critical role in mitigating the systematic bias. Therefore, using all possible interferometric pairs is a realistic and effective solution to mitigate the effect of systematic bias for ALOS or ALOS-2 data.

4.4 Importance of continuous observation
Some areas (e.g., 016 Tomakomai, 151 Niigata, south of 022 Hirosaki) showed similar subsidence in the ALOS (2006–2011) and Sentinel-1 (2014–2020) results, indicating that subsidence has continued for 15 years. However, many areas showed different deformation (i.e., appearance/disappearance, acceleration/deceleration, enlargement/shrinkage). Because the observation periods do not overlap, we cannot know when and how the deformation changed between 2011 and 2014. Although some SAR data are available for this period (e.g., TerraSAR-X,

COSMO-SkyMed, RADARSAT-2), they are not globally available and accessibility is limited (i.e., costly). Long-term, continuous, and uninterrupted availability of global SAR data will make it possible to detect the spatial and temporal evolution of land surface deformation and to understand its mechanisms in detail. The successors of Sentinel-1 A/B (i.e., Sentinel-1 C/D) and many other next-generation SAR satellites (e.g., NISAR and ALOS-4) are planned to be launched soon and will prevent the generation of the blank period of the watchful eyes of SAR from space.

5　Conclusions

In this study, we measured the ground surface deformation in all major urban areas in Japan from 2006 to 2011 using open and free AIST ALOS InSAR products and the open-source InSAR time series analysis tool LiCSBAS. We compared the result with the deformation derived from open and free COMET LiCSAR products based on Sentinel-1 data from 2014 to 2020 (Morishita 2021) and investigated the long-term deformation. As a result, various deformation signals were detected, such as long-term constant subsidence (e.g., 016 Tomakomai and 151 Niigata), changes in deformation areas and/or velocities (e.g., 022 Hirosaki, 121 Kujyukuri, 171 Kanazawa, and 203 Matsushiro), and appearance or disappearance of deformation (e.g., 081 Joso, 132 Yoyogi, and 261 Kyoto).

InSAR time series analysis using SAR data covering the ground surface with a wide swath and high density allows us to measure the long-term deformation extensively and efficiently. While this study revealed 15 years of deformation history, more abundant and uninterrupted SAR data, which will be obtained by future SAR satellites, will achieve even longer and more spatially and temporally detailed deformation monitoring.

Abbreviations

ABCI	AI bridging cloud infrastructure
ALOS	Advanced Land Observing Satellite
AIST	National Institute of Advanced Industrial Science and Technology
AOI	Area of interest
ASTER	Advanced Spaceborne Thermal Emission and Reflection Radiometer
CC	Creative commons
COMET	Centre for the Observation and Modelling of Earthquakes, Volcanoes and Tectonics
CPU	Central processing unit
DEM	Digital elevation model
DID	Densely inhabited district
Envisat	Environmental Satellite
ERS	European Remote-Sensing Satellite
EW	East–west
GACOS	Generic Atmospheric Correction Online Service
GDEM	Global Digital Elevation Model
GPU	Graphics processing unit
GSI	Geospatial Information Authority of Japan
InSAR	Synthetic Aperture Radar Interferometry
LiCSAR	Looking into Continents from Space with Synthetic Aperture Radar

LOS	Line of sight
Mw	Moment magnitude
NISAR	NASA-ISRO SAR
SAR	Synthetic Aperture Radar
SNAPHU	Statistical-Cost, Network-Flow Algorithm for Phase Unwrapping

Supplementary Information

The online version contains supplementary material available at https://doi.org/10.1186/s40645-023-00597-5.

> **Additional file 1: Table S1.** AOI list, frames used in this study and their statistics. **Table S2.** Manually removed interferograms. **Figure S1.** Deformation in 153 Sanjo, Niigata. a and b are the vertical deformation velocities derived from ALOS and Sentinel-1, respectively. The black dashed lines are the boundaries of the DID. The black solid lines denote the 5 mm/year contour lines without the 0 mm/year lines. The gray areas in b denote the rice paddy fields. **Figure S2.** Deformation in 291 Nara. a and b are the vertical deformation velocities derived from ALOS and Sentinel-1, respectively. The black dashed lines are the boundaries of the DID. The black solid lines denote the 5 mm/year contour lines without the 0 mm/year lines. The gray areas in b denote the rice paddy fields. **Figure S3.** Deformation in 431 Kumamoto. a and b are the vertical deformation velocities derived from ALOS and Sentinel-1, respectively. The black dashed lines are the boundaries of the DID. The black solid lines denote the 5 mm/year contour lines without the 0 mm/year lines. The gray areas in b denote the rice paddy fields.

Availability of data and materials

All the ALOS LiCSBAS results generated in this study and the figures (LOS velocities, decomposed vertical and EW velocities, optical images, interferometric network, mask) are available on the ZENODO repository (https://doi.org/10.5281/zenodo.8163882). The AIST ALOS InSAR products are available on the INSAR Browser (https://gsrt.digiarc.aist.go.jp/insarbrowser/index.html). LiCSBASpatch_AIST_ALOS is available on GitHub (https://github.com/yumorishita/LiCSBASpatch_AIST_ALOS). LiCSBAS2 is available on GitHub (https://github.com/yumorishita/LiCSBAS2) and the ZENODO repository (https://doi.org/10.5281/zenodo.7654640). The Sentinel-1 LiCSBAS results are available on the ZENODO repository (https://doi.org/10.5281/zenodo.4029616). The GIS data of the DID and rice paddy fields are available on the Ministry of Land, Infrastructure, Transport and Tourism website (https://nlftp.mlit.go.jp/ksj/index.html). The hypocenter data of the Matsushiro earthquake swarm are available on the Japan Meteorological Agency website (https://www.data.jma.go.jp/eqev/data/bulletin/hypo.html).

Declarations

Competing interests

The authors declare that they have no competing interests.

References

Ansari H, De Zan F, Parizzi A (2021) Study of systematic bias in measuring surface deformation with SAR interferometry. IEEE Trans Geosci Remote Sens 59:1285–1301.https://doi.org/10.1109/TGRS.2020.3003421

Aoki Y, Furuya M, Kato T (2008) Coseismic deformation due to the 2007 Chuetsu-oki earthquake (Mw= 6.8). Earth Planets Space 60:1075–1080. https://doi.org/10.1186/BF03353139

Chaussard E, Amelung F, Abidin H, Hong SH (2013) Sinking cities in Indonesia: ALOS PALSAR detects rapid subsidence due to groundwater and gas extraction. Remote Sens Environ 128:150–161. https://doi.org/10.1016/j.rse.2012.10.015

Chen CW, Zebker HA (2002) Phase unwrapping for large SAR interferograms: statistical segmentation and generalized network models. IEEE Trans Geosci Remote Sens 40:1709–1719. https://doi.org/10.1109/TGRS.2002.802453

Chiba Prefecture (2022) Chiba prefecture leveling survey results. https://www.pref.chiba.lg.jp/suiho/jibanchinka/torikumi/seikaomote.html (**in Japanese**). Accessed 30 Sept 2023

Crosetto M, Solari L, Mróz M et al (2020) The evolution of wide-area DInSAR: from regional and national services to the European ground motion service. Remote Sens (basel) 12:2043. https://doi.org/10.3390/rs12122043

De Zan F, Zonno M, Lopez-Dekker P (2015) Phase inconsistencies and multiple scattering in SAR interferometry. IEEE Trans Geosci Remote Sens 53:6608–6616. https://doi.org/10.1109/TGRS.2015.2444431

Doke R, Harada M, Mannen K et al (2018) InSAR analysis for detecting the route of hydrothermal fluid to the surface during the 2015 phreatic eruption of Hakone Volcano, Japan. Earth Planets Space 70:63. https://doi.org/10.1186/s40623-018-0834-4

Doke R, Kikugawa G, Itadera K (2020) Very local subsidence near the hot spring region in Hakone Volcano, Japan, inferred from InSAR time series analysis of ALOS/PALSAR Data. Remote Sens (basel). https://doi.org/10.3390/rs12172842

Elliott JR, Walters RJ, Wright TJ (2016) The role of space-based observation in understanding and responding to active tectonics and earthquakes. Nat Commun 7:13844. https://doi.org/10.1038/ncomms13844

Fattahi H, Amelung F (2013) DEM error correction in InSAR time series. IEEE Trans Geosci Remote Sens 51:4249–4259. https://doi.org/10.1109/TGRS.2012.2227761

Fujiwara S, Yarai H, Kobayashi T et al (2016) Small-displacement linear surface ruptures of the 2016 Kumamoto earthquake sequence detected by ALOS-2 SAR interferometry. Earth Planets Space 68:160. https://doi.org/10.1186/s40623-016-0534-x

Fujiwara S, Nakano T, Morishita Y (2020) Detection of triggered shallow slips caused by large earthquakes using L-band SAR interferometry. Earth Planets Space 72:119. https://doi.org/10.1186/s40623-020-01239-6

Hashimoto M (2016) Ground deformation in the Kyoto and Osaka area during recent 19 years detected with InSAR. In: International association of geodesy symposia. Springer, pp 155–164

Ishitsuka K, Matsuoka T (2016) Accuracy evaluation of persistent scatterer interferometry using ALOS/PALSAR data: a case study of surface displacement in the Kujukuri Plain, Chiba Prefecture. J Remote Sens Soc Jpn. https://doi.org/10.11440/rssj.36.328

Japan Meteorological Agency (2016) Special site for the 50th anniversary of the Matsushiro Earthquake Swarm. https://www.data.jma.go.jp/eqev/data/matsushiro/mat50/disaster/higai.html. Accessed 29 Jun 2023

Jet Propulsion Laboratory (2020) NASA-ISRO SAR Mission (NISAR). https://nisar.jpl.nasa.gov/. Accessed 22 Jul 2023

Kobayashi T, Tobita M, Nishimura T et al (2011) Crustal deformation map for the 2011 off the Pacific coast of Tohoku Earthquake, detected by InSAR analysis combined with GEONET data. Earth Planets Space 63:621–625. https://doi.org/10.5047/eps.2011.06.043

Kobayashi T, Morishita Y, Munekane H (2018) First detection of precursory ground inflation of a small phreatic eruption by InSAR. Earth Planet Sci Lett 491:244–254. https://doi.org/10.1016/j.epsl.2018.03.041

Lazecký M, Spaans K, González PJ et al (2020) LiCSAR: an automatic InSAR tool for measuring and monitoring tectonic and volcanic activity. Remote Sens (basel) 12:2430. https://doi.org/10.3390/rs12152430

Ministry of Land, Infrastructure, Transport and Tourism (2015) Digital national land information (densely inhabited district). https://nlftp.mlit.go.jp/ksj/gml/datalist/KsjTmplt-A16-v2_3.html (**in Japanese**). Accessed 22 Jul 2023

Ministry of the Environment (2020) Overview of subsidence areas in Japan. https://www.env.go.jp/water/jiban/gaikyo/gaikyo30.pdf (**in Japanese**). Accessed 2 Jul 2023

Morishita Y (2021) Nationwide urban ground deformation monitoring in Japan using Sentinel-1 LiCSAR products and LiCSBAS. Prog Earth Planet Sci 8:6. https://doi.org/10.1186/s40645-020-00402-7

Morishita Y, Hanssen R (2015) Temporal decorrelation in L-, C-, and X-band satellite radar interferometry for pasture on drained peat soils. IEEE Trans Geosci Remote Sens 53:1096–1104. https://doi.org/10.1109/TGRS.2014.2333814

Morishita Y, Lazecky M, Wright TJ et al (2020) LiCSBAS: an open-source InSAR time series analysis package integrated with the LiCSAR automated Sentinel-1 InSAR processor. Remote Sens (basel) 12:424. https://doi.org/10.3390/rs12030424

Motohka T, Kankaku Y, Miura S, Suzuki S (2020) ALOS-4 L-band SAR observation concept and development status. In: International geoscience and remote sensing symposium (IGARSS). Institute of Electrical and Electronics Engineers Inc., pp 3792–3794

Nishimura T, Tobita M, Yarai H et al (2008) Episodic growth of fault-related fold in northern Japan observed by SAR interferometry. Geophys Res Lett 35:L13301. https://doi.org/10.1029/2008GL034337

Nishimura T, Tobita M, Yarai H et al (2008) Crustal deformation and a preliminary fault model of the 2007 Chuetsu-oki earthquake observed by GPS, InSAR, and leveling. Earth Planets Space 60:1093–1098. https://doi.org/10.1186/BF03353142

Nonaka T, Asaka T, Iwashita K, Ogushi F (2020) Evaluation of the trend of deformation around the Kanto region estimated using the time series of PALSAR-2 data. Sensors 20:339. https://doi.org/10.3390/s20020339

Okada A, Tsubokawa I (1970) Vertical deformation associated with the Matsushiro earthquake swarm. Rep Coord Comm Earthq Predict 2:34–40

Okusawa T, Tsukahara H (2001) Origin of deep ground water in the Matsushiro earthquake swarm area. Zisin (j Seismol Soc Jpn 2nd Ser) 53:241–253. https://doi.org/10.4294/zisin1948.53.3_241

Samsonov S (2010) Topographic correction for ALOS PALSAR interferometry. IEEE Trans Geosci Remote Sens 48:3020–3027. https://doi.org/10.1109/TGRS.2010.2043739

Shen SL, Tohno I, Nishgaki M, Miura N (2004) Land subsidence due to withdrawal of deep-groundwater. Lowl Technol Int 6:1–8

Shimada M (2018) Imaging from spaceborne and airborne SARs, calibration, and applications. CRC Press

Sugimoto R, Shimada M, Morishita Y, et al (2021) Interferometric SAR processing using whole ALOS/PALSAR data archive for measuring the global surface deformation. In: 2021 7th Asia-Pacific conference on synthetic aperture radar (APSAR), pp 1–5. https://doi.org/10.1109/APSAR52370.2021.9688342

Tachikawa T, Hato M, Kaku M, Iwasaki A (2011) Characteristics of ASTER GDEM version 2. In: 2011 IEEE international geoscience and remote sensing symposium. IEEE, pp 3657–3660

Tokyo Metropolitan Government (2022) Report of subsidence survey. https://www.kensetsu.metro.tokyo.lg.jp/content/000060342.pdf. Accessed 27 Jun 2023

Wright TJ, Parsons BE, Lu Z (2004) Toward mapping surface deformation in three dimensions using InSAR. Geophys Res Lett 31:L01607. https://doi.org/10.1029/2003GL018827

Yamanaka M, Morishita Y, Osaka Y (2013) Detection of ground subsidence by InSAR time series analysis. J Geospat Inf Auth Jpn 124:1–14

Publisher's Note